Chemical Engineering Journal 316 (2017) 1122–1135

Contents lists available at ScienceDirect

Chemical Engineering Journal

journal homepage: www.elsevier.com/locate/cej

Fabrication of mesoporous CuO/ZrO_2-MCM-41 nanocomposites for photocatalytic reduction of Cr(VI)

Binita Nanda [a,*], Amaresh C. Pradhan [b], K.M. Parida [a,*]

[a] Centre for Nano Science and Nano Technology, Siksha 'O' Anusandhan University, Khandagiri, Bhubaneswar 751030, Odisha, India
[b] UNAM-National Nanotechnology Research Center, Bilkent University, Ankara 06800, Turkey

HIGHLIGHTS

- Mesoporous ZrO_2–MCM-41synthesized by *in situ* incorporation process.
- CuO@ZM-41 synthesized by modification of CuO onto the ZrO_2–MCM-41.
- CuO@ZM-41nacomposite shows semiconductor behavior and mesoporosity.
- High surface area, lower e^- and h^+ recombination are enhancing the photo-reduction.

GRAPHICAL ABSTRACT

Mesoporous nanocomposite (CuO@ZM-41) is synthesized by incorporating mesoporous ZrO_2 (Z) into MCM-41 (M-41) framework followed by loading of CuO by wetness impregnation method. The synergism between CuO and the support material mesoporous ZM-41 and efficient light absorption on the surface of the composite is the key factor for the reduction Cr^{6+} to Cr^{3+} within 30 min time.

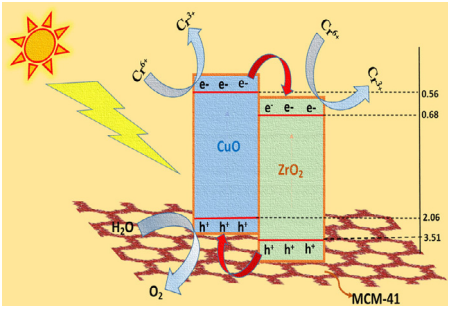

ARTICLE INFO

Article history:
Received 25 July 2016
Received in revised form 12 October 2016
Accepted 10 November 2016
Available online 16 February 2017

Keywords:
CuO/ZrO_2–MCM-41
Nanocomposites
Synergistic effect
Photo-reduction

ABSTRACT

Mesoporous nanocomposites of CuO/ZrO_2–MCM-41 (CuO@ZM-41) was designed by incorporating mesoporous ZrO_2 (Z) into the high surface area MCM-41 (M-41) framework followed by loading CuO by wetness impregnation method keeping Si/Zr ratio 10. The nanocomposites were studied under PXRD, N_2 sorption, DRS spectra, FTIR, XPS, NMR, HRTEM and PL to evaluate structural, morphological, optical properties and also the mesoporosity nature of the samples. The photo-reduction of Cr^{6+} was performed over CuO@ZM-41 by varying pH, substrate concentration, and irradiation time and catalyst dose. Among all the catalysts, 2 CuO@ZM-41 was found to be efficient photocatalyst for the photo-reduction of Cr^{6+}. Nearly 100% reduction of Cr^{6+} has been achieved by 2 CuO@ZM-41 within 30 min. Intra-particle mesoporosity, high surface area, presence of CuO nanorods and electron transfer properties are the key factors for enhancing the photo-reduction activity of 2CuO@ZM-41.

1. Introduction

Over the decade, the extensive use of heavy metal in chemical industries for electroplating, leather tanning, paint processes and mining etc. has become a great concern [1]. It is non-biodegradable, but increases its concentration from one tropic level to other by biomagnification [2]. In nature Cr occurs in a vari-

* Corresponding authors at: Department of Chemistry, Centre for Nano Science and Nano Technology, Siksha 'O' Anusandhan University, Khandagiri, Bhubaneswar 751030, Odisha, India (K.M. Parida).
E-mail addresses: kulamaniparida@soauniversity.ac.in, paridakulamani@yahoo.com (K.M. Parida).

http://dx.doi.org/10.1016/j.cej.2016.11.080
1385-8947/

able oxidation states. Among them, Cr^{3+} has lower toxicity than Cr^{6+} and can be easily precipitated in the form of Cr $(OH)_3$ [3,4]. Various food materials and drinks contain chromium, which is essential for life but it should be within the permissible limit up to 0.1–0.3 mg/L. For body metabolism of plants and animals Cr^{3+} is essential, whereas Cr^{6+} is highly carcinogenic for both of them [5]. Cr^{6+} salts do not easily precipitate [6]. The two divalent oxyanions like chromate (CrO_4^{2-}) and dichromate ($Cr_2O_7^{2-}$) are formed by the dissolution of Cr^{6+} in water body. A suitable method is necessary to remove/reduce the Cr^{6+} from environment. Till date a number of methods like chemical precipitation, reverse osmosis, ion exchange, foam flotation, electrolysis, adsorption etc. are employed for the removal of Cr^{6+} [7–10]. However, most of these techniques need more amount of chemicals and high energy to proceed. Recently, a new technique like photo-catalysis is adopted to decrease/reduce Cr^{6+} concentration from the environment. This process is very safe and quick which has been attracted attention of scientist and enviornmetalist [11,12]. But a challenging factor is that a suitable solid photocatalyst is required for efficient degradation of Cr^{6+} ion from solutions.

In recent years, the scientists and environmentalists have given an attention towards photocatalytic reduction of inorganic contaminants in wastewater through a suitable heterogeneous solid catalyst. Among them, mesoporous materials have attracted a considerable attention because of their high surface area, tunable surface structure [13,14]. The invention of mesoporous siliceous material (MCM-41) is the best studied material having uniform hexagonal array of mesopores and very high surface area (around 1000 m^2/g) [15,16]. For this, MCM-41 (M-41) is considered as an excellent support material. Many scientists have given attention towards the modification of the surface of M-41 to improve the catalytic activity. Till date a number of attempts have been made by substituting various transition metal into the M-41 framework [17,18]. Besides metal substitution, modification of M-41 framework by metal oxide is a challenging task and fascinated by the scientists. This intention increases the textural properties of the amended composite material than neat M-41.

The photocatalysis technology is relatively the finest procedure for the reduction, removal or recovery of dissolved metal ions in wastewater [19]. Various semiconducting materials such as metal oxide used in photocatalytic degradation of Cr^{6+} have been reported. Our group has studied α-FeOOH nanorod/RGO and Gd $(OH)_3$ nanorod/RGO composite for reduction of Cr^{6+} [20,21]. Shrivastava et al. observed the reduction of Cr^{6+}using nanomaterial like TiO_2, ZnO and CdS [22]. Nano structured magnetite in presence of natural surfactant has also been used for reduction of Cr^{6+} [23]. Semiconducting materials like titania pillared zirconium phosphate and sulphate modified titania were used by parida et al. for reduction of Cr^{6+} [24,25]. NH_2 functionalized titanium was also used in reduction of Cr^{6+} [26]. But in our case mesoporous nanocomposites CuO@ZM-41 behaves as a semiconducting-like visible light active photocatalyst for reduction of Cr^{6+} within a small span of time. Moreover, ZrO_2 is one of the most investigated transition metal oxide. Mesoporous ZrO_2 was extensively studied by the scientists in various industrial applications [27–29]. Nanostructured CuO has high catalytic applications due to its high surface-to-volume ration. The CuO will be active species while combining with ZrO_2 and MCM-41. The CuO@ZM-41 may behave as a semiconductor material and which will enhance evolution of electrons in the visible light. The formation and behavior of semiconductor are may be due to the intermixing of localized Cu 2p, Zr 2p and Si 2p orbitals. Hence, the catalytic activity will be increase by the impregnation of Cu(II) onto the surface of mesoporous support ZM-41 (CuO@ZM-41) through synergistic effect of metal to support interaction. This impregnation does not change the structural property, but increases the stability and photocatalytic efficiency.

Herein, we have synthesized a high surface area mesoporous ZM-41 by incorporating mesoporous ZrO_2 into MCM-41 framework (*in situ*) and Cu was impregnated onto the surface of mesoporous support (ZM-41) by varying the different wt% of Cu (2, 4, 6 and 8).The novelty of our work is that nearly 100% of Cr^{6+} was reduced to Cr^{3+} by using 1 g/L 2 CuO@ZM-41 within 30 min under solar light illumination. For optimization of the reaction, the activities of this composite were evaluated under various reaction conditions such as variation of catalyst dose, different substrate concentrations and variable pH etc.

2. Experimental

2.1. Fabrication of mesoporous ZrO_2-MCM-41 (ZM-41)

Mesoporous ZrO_2 (Z) was fabricated first by a sol–gel route by taking zirconium butoxide as the zirconia source and cetyltrimethylammonium bromide (CTAB) as the structure directing agent. The pH of the solution was maintained at 11.5 by ammonium hydroxide solution. The detailed procedure was already given in our previous paper by parida et al. [30]. Mesoporous ZrO_2 was incorporated (*in situ*) into M-41 for the synthesis of mesoporous ZrO_2–MCM-41 (ZM-41). 2.4 g of CTAB was dissolved in minimum amount of deionized water at room temperature. Then Tetraethyl Ortho silicate (10 mL) was added to the solution followed by the addition of NH_4OH under vigorous stirring for 1 h. Mesoporous ZrO_2 was added to the same just before the addition of NH_4OH keeping Si/Zr ratio 10. The resulting solution was filtered and dried at 80 °C for 12 h and calcined at 550 °C for 5 h. The new composite developed called as mesoporous supports ZM-41.

2.2. Synthesis of mesoporous CuO@ZM-41nanocomposites

Mesoporous CuO@ZM-41 nanocomposites were synthesized by wetness impregnation method and Cu $(NO_3)_2$ was taken as the Cu source. The different wt% Cu (2, 4, 6 and 8) was incorporated onto mesoporous support ZM-41 named as X CuO@ZM-41, where X is denoted as the different wt% of CuO. The resulting composites (CuO@ZM-41) were calcined at 600 °C for 6 h. These different composites were named as 2 CuO@ZM-41, 4 CuO@ZM-41, 6 CuO@ZM-41 and 8 CuO@ZM-41. The whole synthetic procedures are shown in Scheme 1.

2.3. Material characterization

The mesoporous nanocomposite CuO@ZM-41 was characterized by XRD, BET surface area, FTIR, XPS, NMR, UV–visible DRS and HRTEM. The XRD patterns were recorded in Rigaku Miniflex (set at 30 kV and 15 mA) powder diffractometer using Cu Kα radiation within the 2θ range from 10 to70° at a rate of 5°/min in steps of 0.01°. The BET surface area was calculated using the adsorption data within the (P/P_o) range from 0.05 to 0.33. The pore volumes were determined at a relative pressure (P/P_o) of 0.95. The Pore size distribution was recorded using desorption branch of isotherm through Barrett-Joyner-Halenda (BJH) modeling. FTIR spectrophotometer (FTS 800) was worked in the range 4000–400 cm^{-1} using KBr wafers. The spectrum was recorded at 4 cm^{-1} resolution with 30 scans. VG Microtech Multilab ESCA 3000 spectrometer with a non-monochromatic Mg-Kα X-ray source was used to record the XPS. Energy resolution of the spectrometer was set at 0.8 eV with Mg-Kα radiation at pass energy of 50 eV. A Gatan CCD camera was used to record the TEM images. UV–vis spectrophotometer was recorded the optical absorption spectroscopy by taking boric acid as the reference.

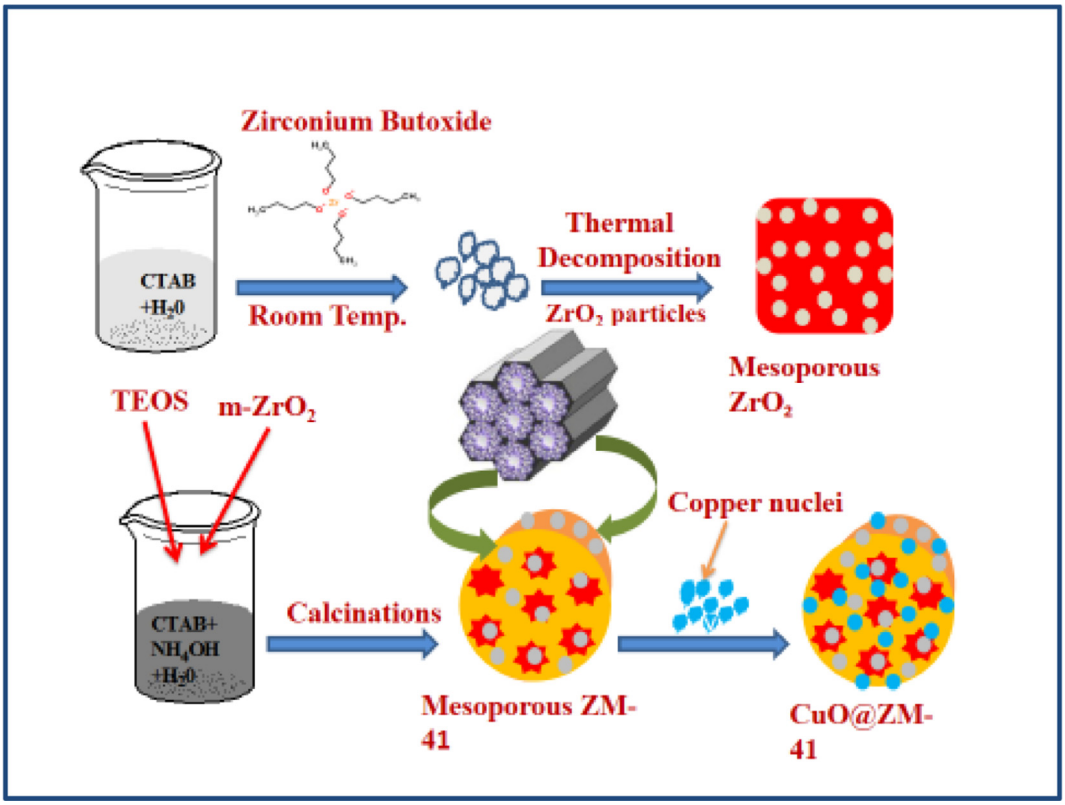

Scheme 1. Schematic representation of the synthesis of nanocomposite CuO@ZM-41.

2.4. Photo-reduction and adsorption of Cr^{6+}

The photo-reduction of Cr^{6+} was done in batch mode reaction procedure by taking 25 mL of 20 ppm of the substrate (freshly prepared $K_2Cr_2O_7$ solution) and 1 g L^{-1} of catalyst. All the photo-reduction experiments were performed in the summer season from 12:00 p.m. to 14:00 p.m. (radiation) at Bhubaneswar, Odisha, India. The average light intensity was around 10 40,000 ± 20 Lx measured by using an LT lutron Lx-101. A digital light meter, which was nearly constant during the experiments. Dilute sulphuric acid or ammonia solution (H_2SO_4, Merck) were used to adjust the pH of the mixture. Three sets of reaction procedure have been carried out. At first the solutions were exposed to sunlight in closed Pyrex flask and stirred continuously with magnetic stirrer, until there is no significant amount of the catalyst remained at the bottom of the flask. Secondly, the adsorption experiment was carried with similar condition, but in the absence of light for 30 min. Lastly, the photolysis experiment was done without catalyst by taking $K_2Cr_2O_7$ solution under visible light irradiation to know the degree of Cr^{6+}reduction. After all the experiments were over, the suspension was filtered and analyzed quantitatively using Varian Cary-1E spectrophotometer with absorption band at 348 nm.

3. Results and discussion

3.1. XRD study

Fig. 1(A) represents the small angle XRD (SAX) arrays of M-41, mesoporous ZM-41 and 2 CuO@ZM-41 respectively. There are three characteristic intensities are indexed. The intense d_{100} diffraction peak indicates the mesoporosity where as other two less intense diffraction peak d_{110} and d_{200} indicates the hexagonal arrangement in periodicity. The SAX of the modified samples (ZM-41 and 2 CuO@ZM-41) including M-41 showed hexagonal arrangement with long range order of pore entrance [18]. But the intensity strongly decreased in the order: M-41 > ZM-41 > CuO@ZM-41. This is due to the incorporation of mesoporous ZrO_2 into M-41 (*in situ*) and loading of CuO onto the surface of ZM-41. The incorporation of different materials into the mesoporous system related with loss of intensity must be attributed to a progressive phase cancellation phenomenon without affecting the long range ordering of M-41 [31].

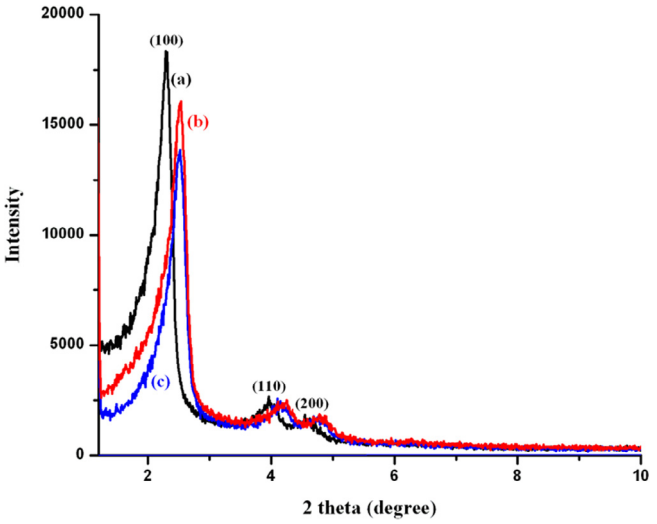

Fig. 1A. (A): Low angle XRD pattern for the samples (a) M-41, (b) mesoporous ZM-41 and (c) CuO@ZM-41.

Fig. 1(B) depicts the broad angle XRD (BXRD) of mesoporous ZrO_2, mesoporous ZM-41 and different wt% of CuO@ZM-41. The sharp intense peak in BXRD pattern suggests the crystalline nature of mesoporous ZrO_2. After the incorporation of mesoporous ZrO_2 into M-41, the intensity gradually decreases. The characteristic *d*-spacing values for reflections due to (101), (110), (011), (002), (112), (200), (211) and (202) planes signifies tetragonal phase of ZrO_2 [32,33]. The incorporation of copper onto the surface of mesoporous ZM-41 possess the crystalline CuO diffraction peaks (35.5^0 and 39.8^0) are assigned to (002) and (111) planes depending on the bulk copper content [34,35]. It is clearly visible that, the diffraction peaks are absent in case of mesoporous ZrO_2 and mesoporous ZM-41.

3.2. BET surface area and BJH pore size measurement

The specific surface area, pore volume and pore diameter of the composite was calculated through the N_2 sorption isotherm and pore size distribution studies. The N_2 sorption isotherm and pore size distribution of mesoporous ZrO_2, mesoporous ZM-41 and 2 CuO@ZM-41 are shown in Fig. 2(A) and (B). It is seen that all the three composites show mesoporosity as N_2 sorption revealed typical type IV isotherm which is well-defined by Brunaueret et al. [36] A steeper N_2 adsorption step in the mid-relative pressure range of 0.30 to 0.45 indicate the relatively intra particle mesoporosity Fig. 2(A). All the materials (mesoporous ZrO_2, mesoporous ZM-41 and different wt% CuO@ZM-41) belong to narrow mesoporous range 2–3 nm. It indicates that all the materials retain intra-particle mesoporosity in BJH pore size measurement.

The different textural properties are derived from N_2 sorption isotherms are shown in Table 1. The surface area of mesoporous ZrO_2 was 80 m^2g^{-1}. After incorporation of mesoporous ZrO_2 into M-41, the high surface area mesoporous ZM-41 (780 m^2/g) obtained. This may be due to M-41 framework modification by mesoporous ZrO_2 without blocking the pores. With these observations, it could be presumed that after incorporation of ZrO_2 into M-41, the Zr(IV) coordinate with Si(IV) giving rise to framework of ZM-41 without breaking mesoporosity. Cu(II) loading may blocks the surface of mesoporous ZM-41, leading to decrease the surface area from 2 CuO@ZM-41to 8 CuO@ZM-41 (Table 1).

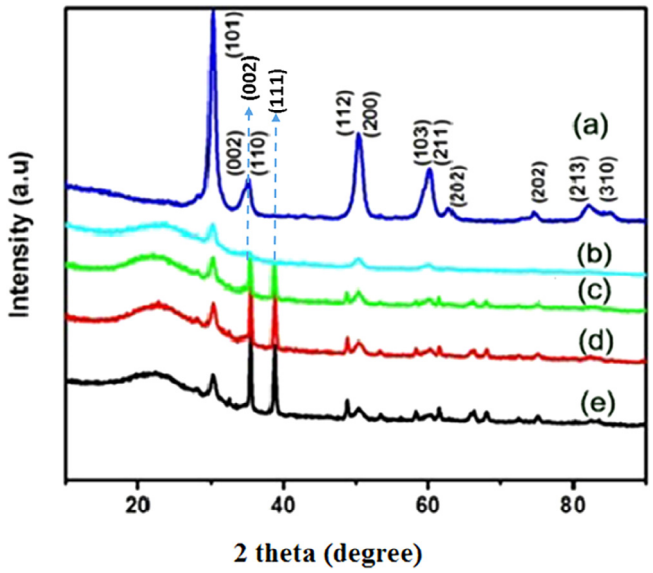

Fig. 1B. (B): High angle XRD pattern for the samples mesoporous ZrO_2, mesoporous ZM-41 (10), 4 CuO@ZM-41, 6 CuO@ZM-41and 8 CuO@ZM-41.

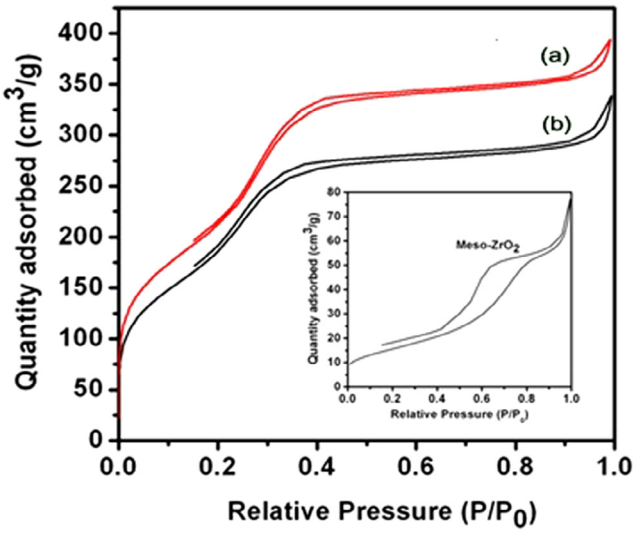

Fig. 2A. (A): N_2 adsorption and desorption isotherm of mesoporous ZrO_2, mesoporous ZM-41, 2 CuO@ZM-41.

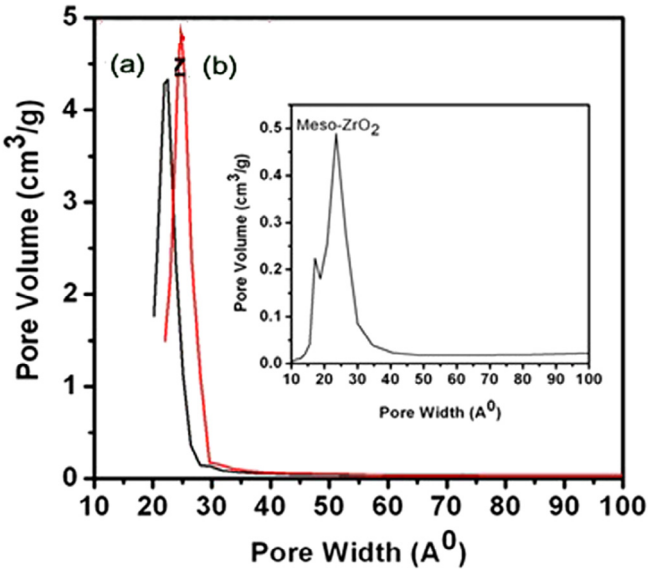

Fig. 2B. (B): Pore size distribution of mesoporous ZrO_2, mesoporous ZM-41and 2 CuO@ZM-41.

Table 1
Textural property of mesoporous ZrO_2, mesoporous ZM-41, 2 CuO@ZM-41 4 CuO@ZM-41, 6 CuO@ZM-41 and 8 CuO@ZM-41.

Samples	Surface area (m^2/g)	Pore volume (cm^3/g)	Pore size (nm)
Mesoporous ZrO_2	80	0.1192	2.32
Mesoporous ZM-41	780	0.6101	2.50
2 CuO@ZM-41	700	0.5239	2.20
4 CuO@ZM-41	625	0.4867	2.35
6 CuO@ZM-41	520	0.3721	2.22
8 CuO@ZM-41	380	0.2876	2.15

The pore volume of ZM-41 was slightly higher than M-41. That means during incorporation of ZrO_2 into M-41 framework, the porosity does not break, rather it maintains the orderliness and intra particle mesoporosity.

3.3. FTIR study

Fourier Transform Infrared spectra of mesoporous ZM-41, and Cu impregnated CuO@ZM-41 (2, 4, 6 & 8 wt%) are shown in the supporting information (Fig. SI 1). For every sample, the peaks at 3200–3700 cm^{-1} are ascribed to stretching vibration mode of –OH group. A medium band near 1634 cm^{-1} is due to the water of hydration assigned to H-O-H bending motion. The band near 1043–1240 cm^{-1} is due to the Si-O asymmetric stretching vibration in Si-O-Si, is common in all the composites except mesoporous ZrO_2. A spectrum clearly shows a band around 964 cm^{-1}, assigned to Si-O vibration in Si-OH group in M-41 [35]. But the peak intensity gradually reduced due to the incorporation of ZrO_2 (Z) and followed by the Cu metal in the framework of MCM-41. It confirms from the shoulder peak at 963 cm^{-1} which is assigned to the stretching vibrations of surface Si-O-Cu bond [37]. This is generally considered to be a proof of the incorporation of metal into the MCM-41 framework. That means, the formation of -O- group from –OH groups is confirmed. Similar results using other metal like Fe, Co, Ni and Zn etc. impregnated MCM-41 was observed by Srinivas et al. [38] Another small Cu–O stretching peak at 660 cm^{-1} is shown only in case of 8 CuO@ZM-41 as Cu concentration is maximum in the sample but it is negligible in all other Cu modified samples. The band near 501 cm^{-1}indicates the presence of both tetragonal and monoclinic zirconia in the composite [32,33].

3.4. HRTEM study

A high resolution of TEM image of ZrO_2 nanocrystal is depicted in Fig. 3(a), (b) and (c). The figure depicts that the particles are well separated from each other. Fig. 3(a) describes the particle size of mesoporous ZrO_2. The single particle size of ZrO_2 was found to be 91 nm. Fig. 3(b) shows the mesoporosity of the ZrO_2. The strong ring patterns from the SAED as shown in the Fig. 3(c). The lattice plane (1 1 0), (0 1 1) and (0 0 2) was indexed to be tetragonal phase [39]. The HRTEM images suggested that mesoporous ZrO_2 was crystalline as reported in XRD studies. After incorporation of ZrO_2 into M-41 and CuO onto the mesoporous support ZM-41, the mesoporosity does not disturb which is revealed in the Fig. 4(a), (b) and (c). Fig. 4(a) attributes the nanorod like structure having average rod diameter 35 nm and length 150 nm and porous nature of 2 CuO@ZM-41. The formation of nanorod might be due to the growth of porous particles in one dimensional direction. Fig. 4 (b) shows the single nanorod having diameter of 25 nm. Lastly, Fig. 4(c) shows the SAED picture of mesoporous nanocomposite 2 CuO@ZM-41. From this picture, it is clearly visible that well-ordered crystal and the line (inset in Fig. 4(c)) indicate the formation of nanorod in the 2 CuO@ZM-41. The energy-dispersive X-ray analysis of 2 CuO@ZM-41 is shown in the Supporting Information (Fig. SI 2). The EDX analysis tells about the existence of Cu, Zr, and Si in mesoporous 2 CuO@ZM-41 nanocomposite.

3.5. XPS study

Incorporation of mesoporous ZrO_2 into M-41 and CuO-modified mesoporous ZM-41 were studied by X-ray photoelectron spectroscopy. It depicts the electronic environment and oxidation state of the entire transition metal ion involved and their relative composition in the composites. The different X-ray photo electron bands of Zr 3p, Si 2p, Cu 2p, and O 1 s core levels are given in

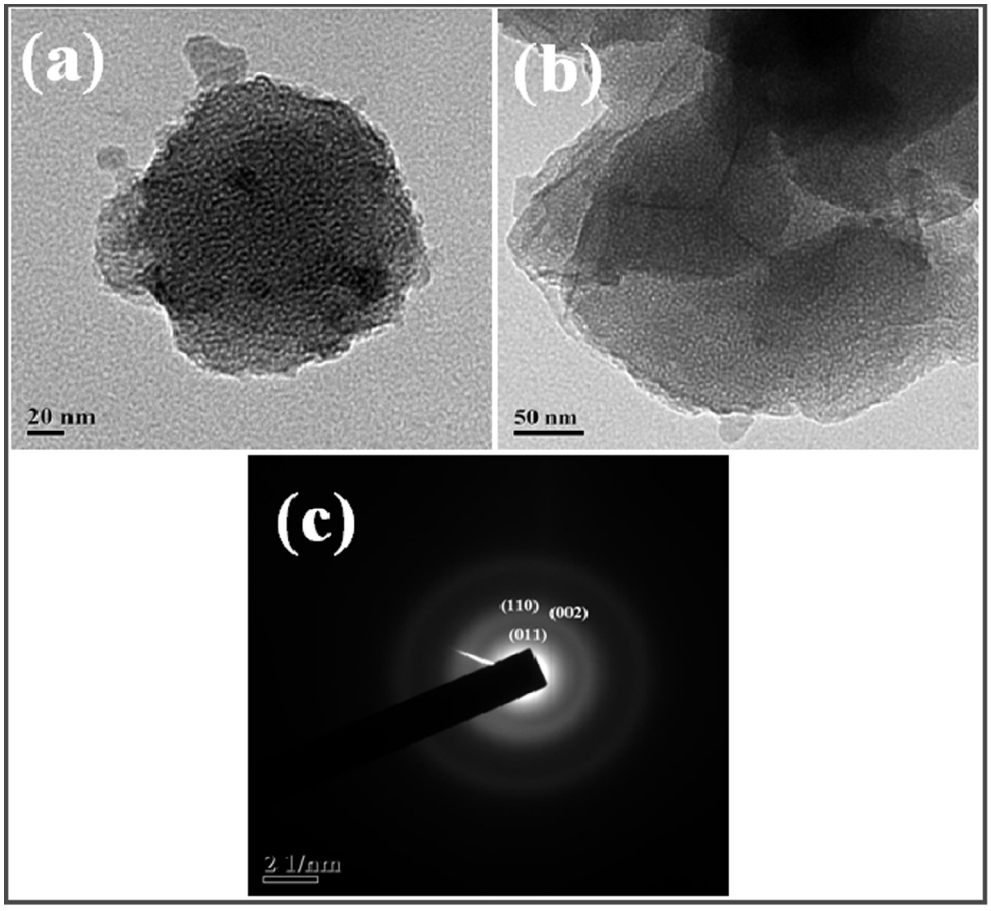

Fig. 3. HRTEM picture of (a) particle size of mesoporous-ZrO_2 (b) mesoporous nature of ZrO_2 (c) SAED of tetragonal ZrO_2.

Fig. 5. The BE of Si 2p in pristine SiO_2 and Zr 3p in ZrO_2 is 103.5 and 346 eV, respectively [40,41]. After incorporation of ZrO_2 into M-41 and Cu immobilized onto the surface of mesoporous ZM-41, the BE of Si 2p shifts to 104.2 eV. At the same time BE of Zr 3p shift towards lower value 339.28 eV. The shifting of binding energy may be due to the strong co-ordination between Zr^{4+} and Si^{4+} through O atom. Thereby, it is resolved that a Si-O-Zr network built in mesoporous ZM-41. The BEs of O 1s was 547 eV, which is slightly more than the reported value (532 eV) [42]. This is because electrons transfer from Si to Zr through oxygen atom. In this present study, the BEs of Cu 2p is found to be at 946.1 eV, suggesting that Cu is in 2+ oxidation state. Previously it has been reported that the BEs of Cu is 933 eV [42]. The BEs of Cu moves towards higher values and at the same time Zr 3p towards the lower values indicating the strong metal-support interaction.

3.6. DRS spectra

The DRS spectra of mesoporous ZrO_2, mesoporous ZM-41 and of CuO@ZM-41 (different wt%) composites are shown in Fig. 6(A). Mesoporous ZrO_2 shows a strong absorption band at 210–320 nm, and there is a charge transfer occurred from the oxide species to the zirconium cation ($O^{-}\rightarrow Zr^{4+}$). All the composites exhibit a broad absorption band near 270 nm. It might be due to LMCT between surface O and isolated Cu^{2+} ions [43]. By loading the copper (different wt%) onto mesoporous ZrO_2, a broader charge transfer band of Cu ions formed by showing an additional shoulder peak at 340 nm. That means a small amount of CuO cluster was formed in highly dispersed state. Abroad charge transfer transition band and a shoulder peak at 310–350 nm was observed by Shimokawabe et al. [44]. In CuO@ZM-41, the d-d transition band for octahedral coordinated Cu^{2+} species was observed in the visible region 700–800, showing high photocatalytic reduction. But this band was absent in ZM-41, representing lower percentage of reduction in visible light region. The following equation was used to evaluate the band gap energy of a semiconductor [45].

$$\alpha h\upsilon = A(h\upsilon - Eg)^n$$

where, α, υ, A, and Eg are considered as the absorption coefficient, frequency of light, proportionality constant and band gap energy respectively. The values of n show the characteristic of transitions. For direct transition it is ½ and for indirect transition it is 2 [45]. It was found that mesoporous ZM-41 and the composite CuO@ZM-41 show direct allowed transitions. Fig. 6(B) depicts the band gap energy of all the composites. All the plots are calculated by plotting $(\alpha h\upsilon)^n$ vs. hυ. A straight lines are extrapolated to the hυ axis and the band gap energy of mesoporous ZM-41 was found to be 3.47 eV. After incorporation of CuO onto the surface of ZM-41, the energy reduces to 1.68 eV. This might be due to the formation of a localized state by mixing of Cu 2p, Zr 3p and Si 2p. Again the band gap energy slightly reduces from 1.68 eV to 1.37 eV as we move from 2 CuO@ZM-41 to 8 CuO@ZM-41. The band gap energy of different composites are (2 CuO@ZM-41 = 1.68 eV, 4 CuO@ZM-41 = 1.48 eV, 6 CuO@ZM-41 = 1.40 eV and 8 CuO@ZM-41 = 1.37 eV). As we increase the percentage of Cu onto the surface of support material, it leads to narrowing the band gap energy and red shift occur. This band gap narrowing is the emerging of the impurity (CuO) band formed by the overlapped impurity states. Hence, all the composites (2 CuO@ZM-41 to 8 CuO@ZM-41) are visible light active semiconducting material.

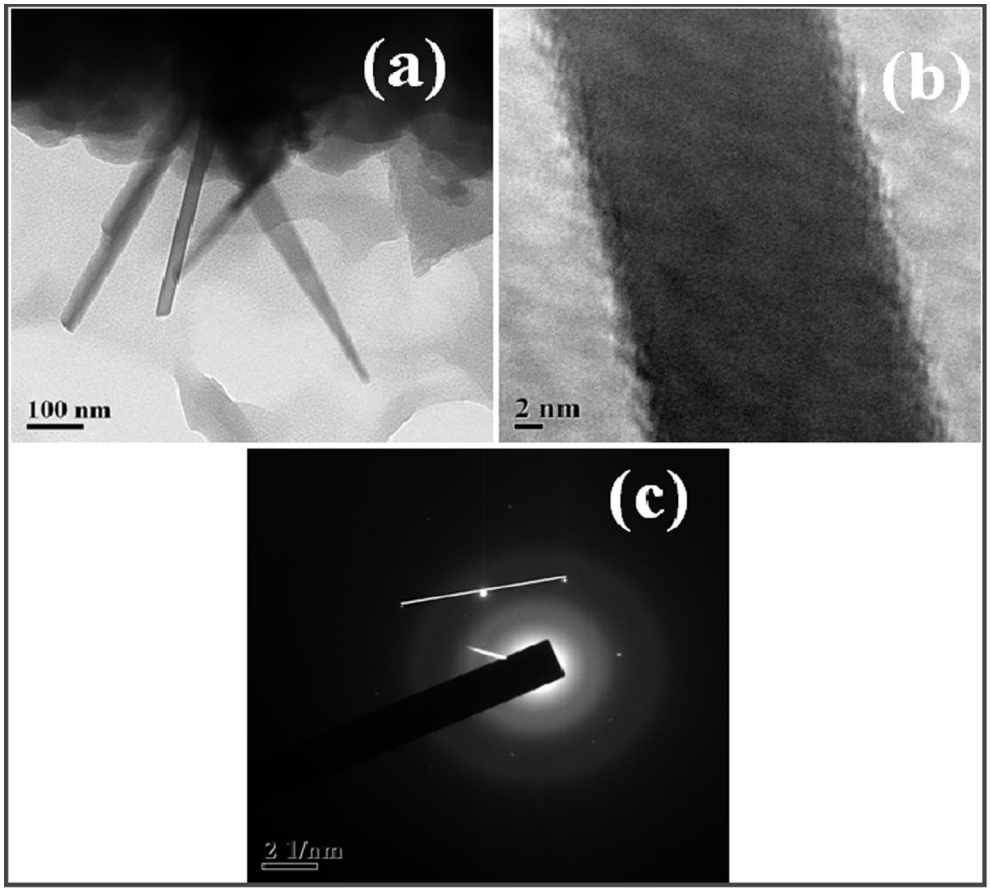

Fig. 4. HRTEM of (a) 2 CuO@ZM-41 (b) nanorod structure of 2 CuO@ZM-41and (c) SAED of 2 CuO@ZM-41.

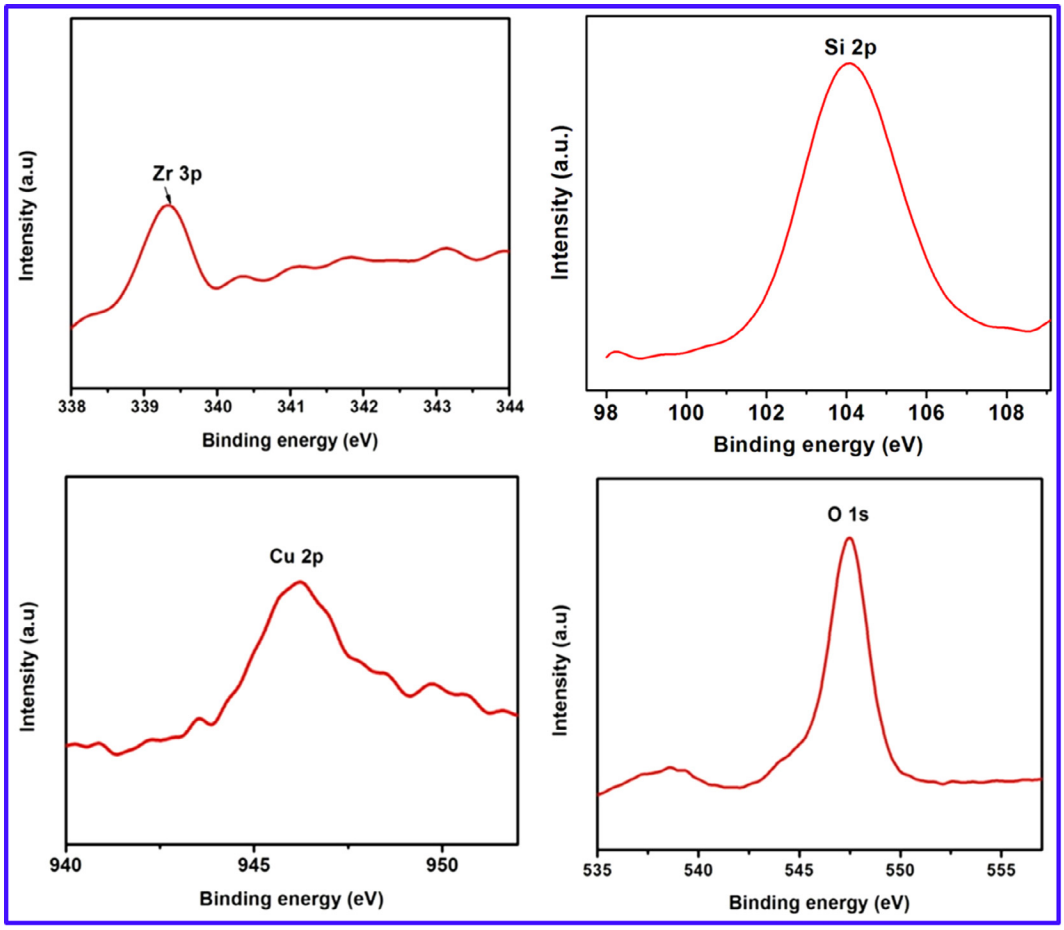

Fig. 5. Representative XPS core-level spectrum of Zr 3p, Si 2p, Cu 2p and O 1sin 2CuO@ZM-41.

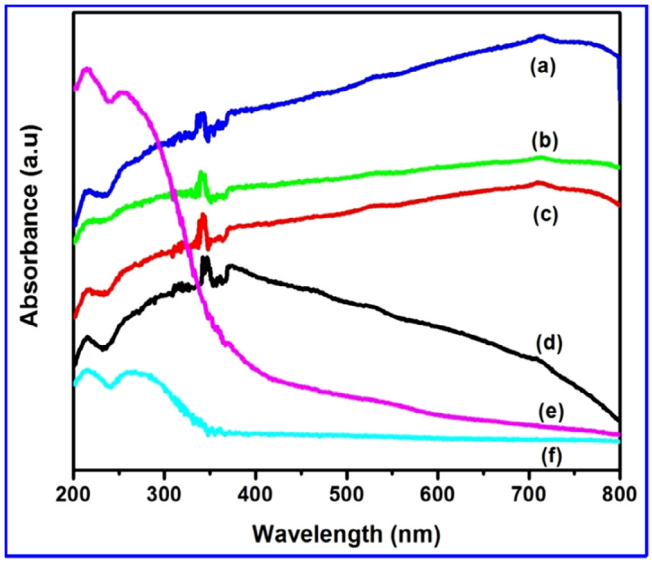

Fig. 6a. (a): UV–Vis DRS spectra (a) 8CuO@ZM-41, (b) 6CuO@ZM-41, (c) 4 CuO@ZM-41, (d) 2CuO@ZM-41, (e) mesoporous ZrO_2 and (f) mesoporous ZM-41.

3.7. NMR study

The Nuclear magnetic resonance study is performed to know the co-ordination of mesoporous ZrO_2 with MCM-41 (M-41) and to ensure the hydrolysis of zirconium butoxide mainly occur on the surface of M-41. Fig. 7(a) and (b) depicts the resonance spectra of M-41 and CuO@ZM-41. For neat M-41, illustrates the broader peak near −111, −103, and −94 ppm ascribed to Q^4resembles to Si $(OSi)_4$; Q^3 to $(SiO)_3$ Si OH and Q^2 to $(SiO)_2$ Si $(OH)_2$, respectively. But after incorporation of Cu onto the mesoporous ZM-41 (CuO@ZM-41), the peak was slightly shifted and observed at −113.1, −104 and −94.5 resembles to Q^4, Q^3 and Q^2, respectively. The slightly shifting of intensities indicates the coordination of Zr (IV) with Si(IV) through oxygen atom in the framework of M-41 channel.

3.8. Photo-reduction of Cr^{6+}

3.8.1. Variation of initial concentration

The rate of photo-reduction of Cr^{6+} was done by varying the initial concentration of Cr^{6+} within 2–50 mg L^{-1} over the catalyst 2 CuO@ZM-41 was explained in the supporting information (Fig. SI 3) depicts that, at first within the concentration 2–5 mg L^{-1} Cr^{6+} was reduced nearly 100%. But the photo-reduction% gradually decreases with increase in initial concentration 10–50 mg L^{-1}. This is reduced from nearly 100% to 43%. As the catalyst dose is same throughout the reaction process, active sites for the photo-reduction process remaining the same. When the substrate concentration is more than that of the catalyst then the light absorption may be more. As the catalytic active sites remain same, the photo-reduction of Cr^{6+} may not be effective. For this reason with increase the substrate concentration, photo-reduction of Cr^{6+} decreases.

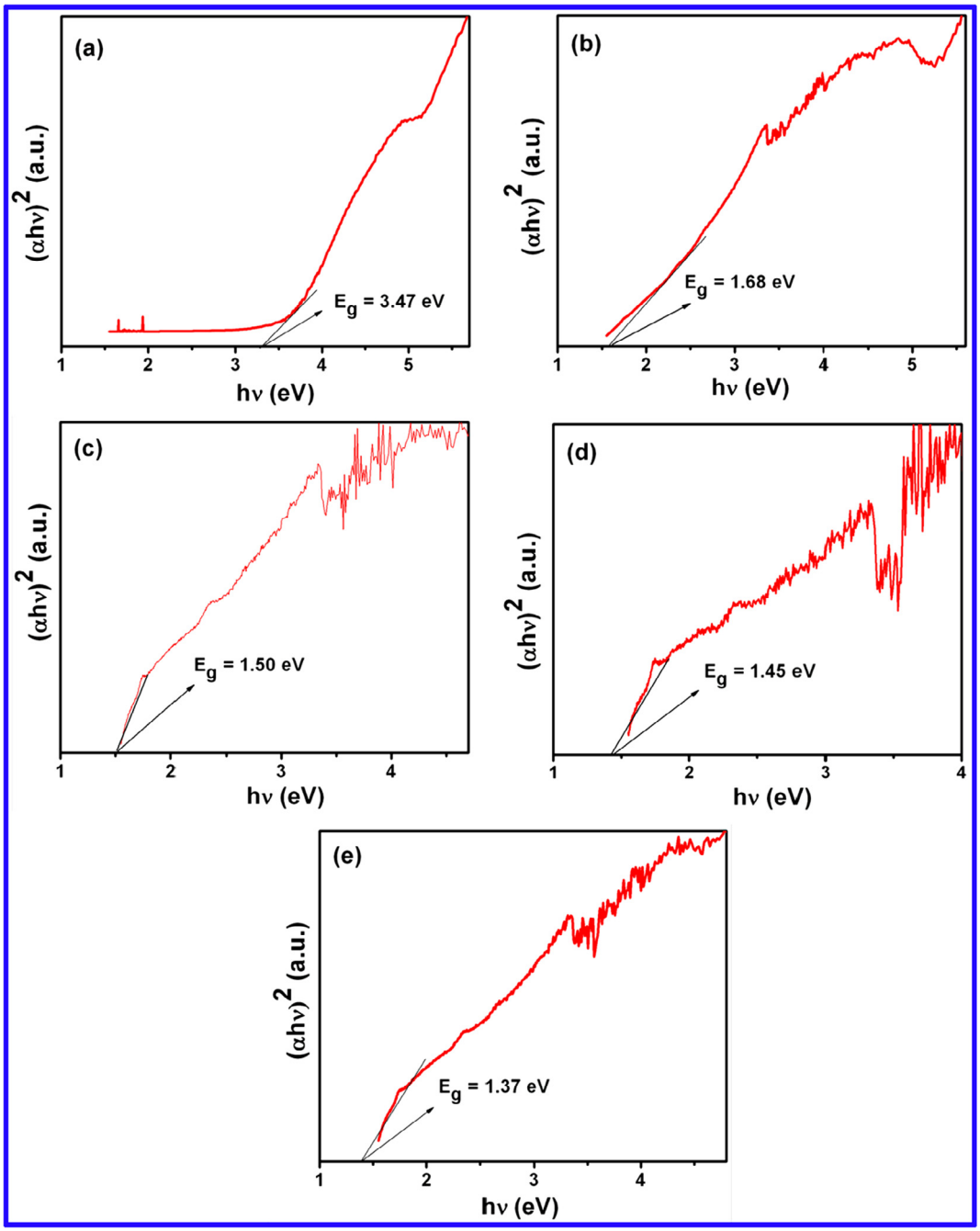

Fig. 6b. (b): Plots of $(\alpha h\upsilon)^n$ vs. photon energy ($h\upsilon$) for the band gap energy of (a) mesoporous ZM-41, (b) 2 CuO@ZM-41, (c) 4 CuO@ZM-41, (d) 6 CuO@ZM-41 and (e) 8 CuO@ZM-41.

3.8.2. Variation of catalyst dose

The photo-reduction rate of Cr^{6+} was done with variable 2 CuO@ZM-41 concentration from 0.4 to 1.6 g L^{-1} and explained in supporting information (Fig. SI 4). It was observed that by increasing the catalyst dose up to 0.8 g L^{-1}, the photo-reduction (%) gradually increases and thereafter it remains almost constant. It is due to the fact that when concentration of the catalyst increases, then the photon absorption increases. So, more number of reacting molecule of Cr^{6+} adsorbed on the surface of the composite. But it is seen that with higher catalyst dose (i.e. >0.8 g L^{-1}) there is no further reacting molecules available for adsorption of Cr^{6+}. That means the additional catalysts are not used in the reaction process. For this, we have taken a constant catalyst dose (1 g L^{-1}) throughout the reaction process.

3.8.3. pH variation

The removal of $Cr^{6+}$from aqueous solution depends strongly on pH. The experiment was carried out with variation of pH from 4 to 10, catalyst dose 1 g L^{-1}, Cr^{6+} concentration (20 mg L^{-1}) in the presence of sunlight for 30 min time. The highest reduction rate was possible at lower pH 4. Fig. 8 depicts the effect of pH on the mesoporous nanocomposite 2 CuO@ZM-41in the pH range 4–10. It is observed that with increasing pH up to 10, the photo-reduction (%) gradually decreases. The photo-reduction of Cr^{6+} depends on the percentage of adsorption of Cr^{6+} on the surface of the catalyst. That means when there is more adsorption, more photo-reduction takes place [41]. Cr^{6+} solution mainly exists in three different forms i.e. H_2CrO_4, $HCrO_4^-$ and $Cr_2O_7^{2-}$ respectively. They can be transferred to each other with change in pH [24].

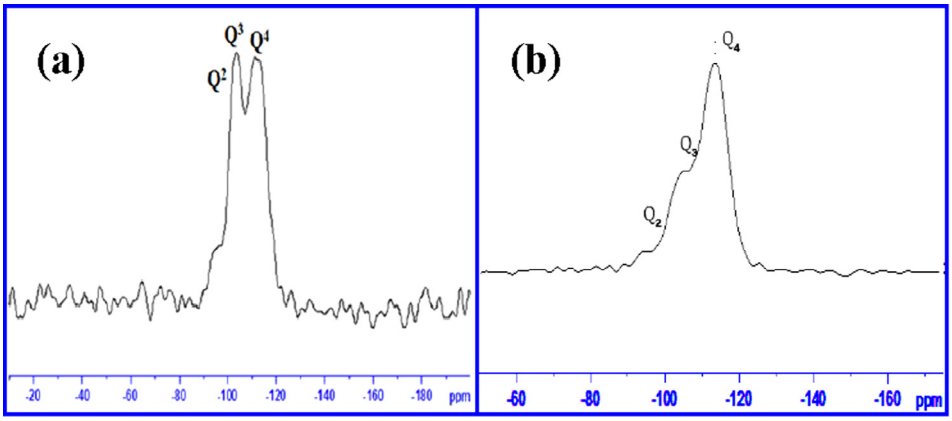

Fig. 7. ^{29}Si CP-MAS NMR spectra of (a) M-41 and (b) 2 CuO@ZM-41.

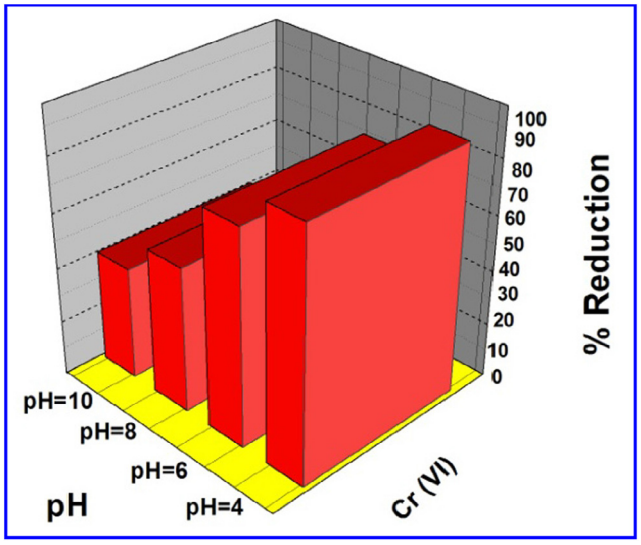

Fig. 8. Effect of pH on the percentage of Cr^{6+}reduction on 2 CuO@ZM-41. The pH varied from 4 to 10. The reaction was preceded by taking 1.0 g L^{-1} of catalyst. The reaction was carried out in the presence of sunlight and at room temperature for 30 min.

Cr^{6+} species exists as $HCrO_4^-$in acidic medium and as CrO_4^{2-} in neutral or basic medium. Cr^{6+} in solution exhibit the following equilibrium state [24].

$$H_2CrO_4 \rightarrow HCrO_4^- + H^+ \quad pKa = 1.2 \tag{1}$$

$$HCrO_4^- \rightarrow CrO_4^{2-} + H^+ \quad pKa = 6.52 \tag{2}$$

Cr^{6+} was reduced more in acidic medium than neutral or basic medium was reported earlier [23]. The reasons are

i) In acidic medium, the surface of the photocatalyst becomes highly protonated and increases the charge on the surface, which resulted in stronger electrostatic force of attraction for $HCrO_4^-$ (chromium anions). As a result there is a strong electrostatic force of attraction between Zr^{4+} and $HCrO_4^-$ ion. The adsorption of chromium onto the surface of CuO@ZM-41 nanocomposite is more at pH 4 and creates a better platform for photochemical process. At higher pH, the surface of the composite become negatively charged and repels the chromium anion and decreases the photo-reduction activity.

ii) This can also be proved through the isoelectric/point zero charge (pHpzc). It determines the surface charge of the composite [46]. The pHpzc value of CuO modified mesoporous ZrO_2-MCM-41 (CuO@ZM-41) was found to be 4.5. At pH lower than the pHpzc value, there will be more positive charge ions around the composite, enhancing adsorption of more number of $HCrO_4^-$ ions, thus resulting in enhancement in Cr^{6+} reduction. When the pH is more than pHpzc, the surface of the composite is negatively charged and decreasing the adsorption of $HCrO_4^-$ due to electrostatic force of repulsion resulting in decrease in photo-reduction of Cr^{6+}.

3.8.4. Photolysis, control experiments and photocatalysis

Three different sets of photocatalytic experiments were done by taking mesoporous 2 CuO@ZM-41. The experiments were carried out by taking Cr^{6+} (20 mg L^{-1}), catalyst dose (1 g L^{-1}) at pH 4 for 30 min of reaction time are shown in Fig. 9. Initially, photolysis reaction was proceeded in the absence of photocatalyst, but in presence of solar light. A less amount of Cr^{6+} reduction took place. Secondly, the control experiments were done in absence of light for 30 min. It indicates that Cr^{6+} was adsorbed on the active sites of the catalyst. The equilibrium state of Cr^{6+} adsorption was reached within 10 min. The Cr^{6+} adsorption percentage was recorded by the following order: 2 CuO@ZM-41 (27%) > 4 CuO@ZM-41 (22%) > 6 CuO@ZM-41 (18%) > 8 CuO@ZM-41 (15%) > mesoporous ZM-41 (12%) > M-41 (9%) > ZrO_2 (6%) which is commensurate with that of surface area. Lastly the photocatalysis experiment was carried out under solar light. During the visible light irradiation on the mesoporous nanocomposite (CuO@ZM-41), electrons are ejected from VB to CB and created photo excited electrons (e−) in CB and hole (h^+) in VB. These excited electrons (e−) help in photo-reduction of Cr^{6+} to Cr^{3+}. At the same time the hole (h^+) created in CB oxidize the surface hydroxyl molecule to O_2. All four CuO@ZM-41 nanocomposites including mesoporous ZrO_2 and mesoporous ZM-41 showed higher photo-reduction of Cr^{6+} as compared to photolysis and control experiment. From the experimental data it is shown (Fig. 4) that nearly 100% Cr^{6+}reduction took place on 2 CuO@ZM-41 as the adsorption efficiency is higher than other composites and reduction efficiency gradually decreases from 2 to 8 wt% CuO@ZM-41 i.e. 2 CuO@ZM-41 (99%) >4 CuO@ZM-41 (95%) > 6 CuO@ZM-41(91%) > 8 CuO@ZM-41 (89%). This is because in 2 CuO@ZM-41, a small amount of copper was dispersed on the high surface area of the support ZM-41. This increases the surface active sites than other modified composites. The surface area of 2 CuO@ZM-41 is also higher to absorb Cr^{6+} onto its surface and thereby increases the photo-reduction activity. But in case, M-41 and ZM-41 the reduction activity are restricted

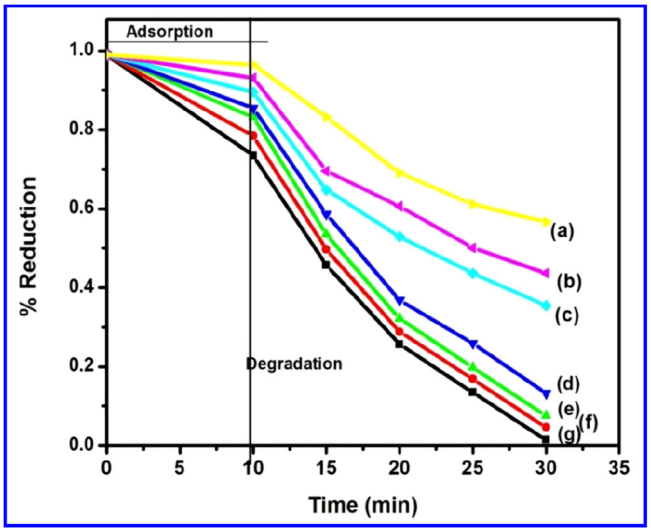

Fig. 9. Photolysis, adsorption and photo reduction of Cr^{6+}in aqueous solution (20 mg L^{-1}), 30 min time interval with all as prepared (a) M-41, (b) mesoporous ZrO_2, (c) mesoporous ZM-41, (d) 8 CuO@ZM-41, (e) 6 CuO@ZM-41, (f) 4 CuO@ZM-41and (g) 2 CuO@ZM-41.

because of easy electron-hole recombination. Though photo-reduction activity is carried out in the lower concentration there is a greater possibly for the Cr to be present in its CrO_4^{2-} form. The photo-reduction of Cr^{6+} on the mesoporous nanocomposite at pH 4 is described in the following equation:

$$CuO@ZM - 41 + h\upsilon \rightarrow e^-_{(CB)} + h^+_{(VB)} \quad (3)$$

$$h^+_{(VB)} + H_2O(OH^-) \rightarrow OH^{\cdot} \quad (4)$$

$$CrO_4^{2-} + 8H^+ + 3e^-_{(CB)} \rightarrow Cr^{3+} + 4H_2O \quad (5)$$

$$2H_2O \rightarrow O_2 + 4H^+ + 4e^- \quad (6)$$

The net reaction is as follows

$$4CrO_4^{2-} + 20H^+ \rightarrow 4Cr^{3+} + 10H_2O + 3O_2 \quad (7)$$

3.8.5. Mechanism

The photo-reduction activity of the composite (CuO@ZM-41) is explained by Scheme 2. When the material was exposed to solar light (UV–Visible) irradiation, both CuO (p-type semiconductor with band gap 1.5–2.2 eV) and ZrO_2 (n-type semiconductor with band gap 4.0–7 eV) have the capability to absorb photons to produce photo-generated electrons (e^-) and holes (h^+) which are effectively transferred at the interface to reduce their recombination [47]. The conduction band (CB) and valence band (VB) potentials of CuO and ZrO_2 can be calculated by the Eq. (8)

$$E_{CB} = X - Ec - 1/2(Eg) \quad (8)$$

where X is the absolute electro negativity of semi-conductor which is calculated from the absolute electro negativity of the constituent atoms, Ec ~4.5 eV (energy of free electrons measured on the hydrogen scale) and Eg is the band gap of the semiconductor. The conduction band and valence band potential of ZrO_2 are +0.68 V and +3.1 V and those of CuO are found to be +0.56 V and +2.06 V respectively. As the position of CB of ZrO_2 is more positive than CuO, the photo-generated electrons on the CuO can transfer easily from CB of CuO to CB of ZrO_2 [48]. As a result there is an accumulation of photo-generated electrons in the conduction band of ZrO_2, which may responsible for photo-reduction of Cr^{6+}. Form this; it is clear that efficient light absorption on the surface of the composite is the key factor for the reduction Cr^{6+} to Cr^{3+}. Apart from this, the activity is also attributed to the supporting MCM-41 surface, well dispersed visible light active Cu metal on the outer wall surface of ZM composite. The strong association with CuO and ZrO_2 further facilitates UV–visible light absorption, charge transport and improves the photo-reduction performance of the catalyst.

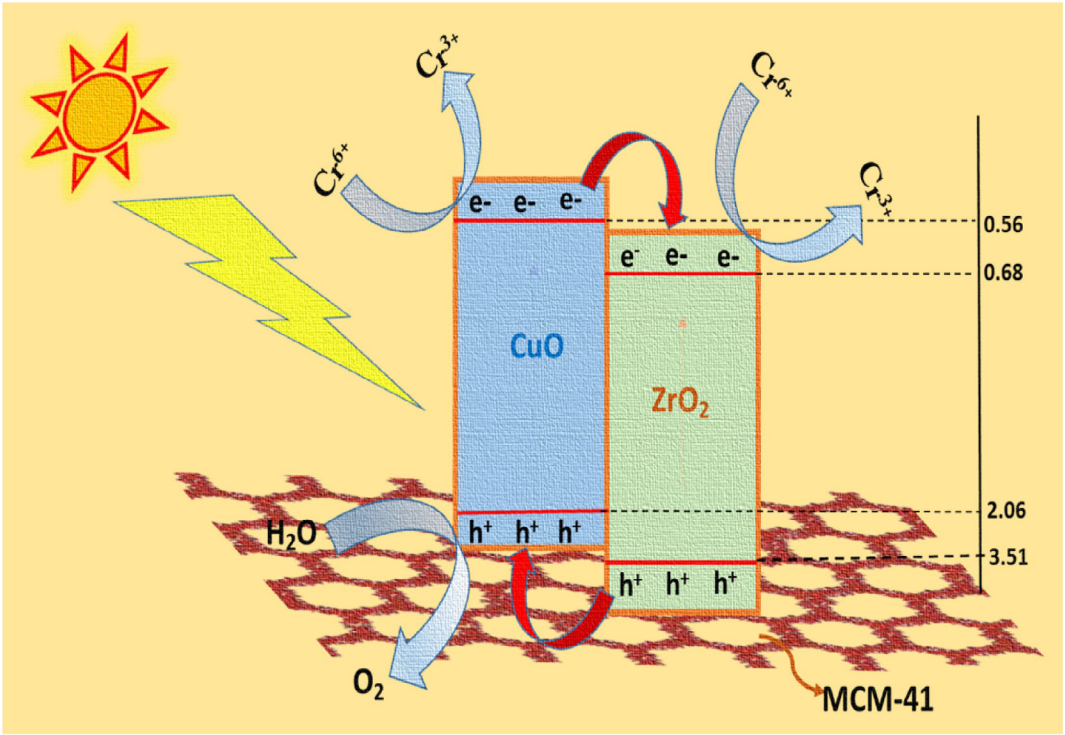

Scheme 2. Schematic representation of photo-reduction of nanocomposite CuO@ZM-41.

3.9. Factors affecting the enhancement of photo-reduction activity on CuO@ZM-41 nanocomposite

The enhancement of photo-reduction activity of CuO@ZM-41 nanocomposite mainly depends on the following factors i.e. (1) Surface morphology; (2) synergistic effect of Cu with support material mesoporous ZM-41; (3) lowering the electron-hole recombination.

(1) Surface morphology

Surface area plays a significant role in the photocatalysis is because it reveals the concept of adsorption of substrate molecule onto the surface of the catalyst. When surface area increases the number of surface anchoring sites of the catalyst is also increases. This leads to better adsorption of substrate molecule on the surface of the catalyst and converts to byproduct. In this present study, the specific surface area of mesoporous ZrO_2 is observed to be 80 m^2/g. But when mesoporous ZrO_2 was incorporated into M-41 framework (*in situ*), there is a significant change in specific surface area, pore volume and pore diameter (Table 1). This may be due to the reversible coordination between Zr and Si atom forms Zr-O-Si bond. It has been observed that MnO_2–MCM-41 surface area increased efficiently by the reversible coordination between the Mn and Si.[45] This increases the surface anchoring sites of the sample and reduction will be more. However, after incorporation of CuO onto the surface of mesoporous ZM-41, some of the Cu particle may deposit on the surface of ZM-41 and decreases the surface area slightly. But it was observed that in all the CuO modified ZM-41composites showed higher percentage of photo-reduction. This is because all the composites having small particle size i.e. less than 100 nm (nanoparticle). In case of CuO@ZM-41 is nanorod like structure having length 70 nm and breadth 30 nm is confirmed from TEM (Fig. 4). That means the high specific surface area, small particle size, narrow pore diameter and wide pore volume leads to enhance the availability of surface anchoring sites for the accommodation of substrate molecule. (See Table 2)

(2) Synergistic effect of Cu with mesoporous ZM-41

Metal incorporation onto the surface of the support material increases the surface anchoring sites for catalytic application. It is perceived that when Cu^{2+} was incorporated onto the surface of ZM-41 i.e. CuO@ZM-41, was very stable after calcination at (600 °C for 6 h) and the oxidation state remain unchanged, was confirmed from XPS analysis. The easy dispersion of CuO particles onto the 2-D flat surface of ZM-41 forms a strong bond between Cu^{2+} and the support material and (ZM-41). The well decoration of Cu particles on the ZM-41 (CuO@ZM-41), establishes the synergism by the strong attachment which gives rise in enhancing photo-reduction capacity. This easy dispersion is due to the extremely high surface area, wide pore volume and narrow pore diameter, and increases the photo-reduction capacity of Cr^{6+}. In previous paper we have reported Cu dispersion within silica and mesoporous Al_2O_3 favors radical mechanism [35]. Likewise, in our present study Cu dispersion on the surface of mesoporous ZM-41 leads to (a) mobilization of electrons to its surface, (b) sinking of photoexcited electron for lowering the electron hole recombination, (c) enhancement of photo-reduction capacity of Cr^{6+} to Cr^{3+}.

(3) Lowering of electron-hole recombination

Photo luminescence emission spectra describes the migration, charge transfer carriers to the surface the composite and the of electron-hole pair recombination in the semiconductor catalysts. PL emission spectra can record the separation capacity of the photo-induced charge carriers and improve the quantum yield of the photocatalyst [49]. Hence, there is a minimum electron-hole recombination found in a noble material. To know the electron-hole recombination of charge carriers, Fig. 10 depicts the photo luminescence spectroscopy of all the composites at room temperature with an excitation of 400 nm. Photoluminescence emission intensity is directly interrelated to recombination of excited electron and hole [50]. Greater the photo luminescence intensity, the greater is the recombination of the charge carriers, results into less photo-reduction activity. It is observed from the result that the composite material (2 CuO@ZM-41) has lower photo luminescence intensity than the support mesoporous ZM-41 and ZrO_2. Mesoporous ZrO_2 exhibits an intense peak at 422 nm. The decrease in PL intensity is due to the incorporation of ZrO_2 into M-41 framework (ZM-41) and the modification of CuO onto the surface of mesoporous ZM-41.The incorporation metal oxides facilitate the

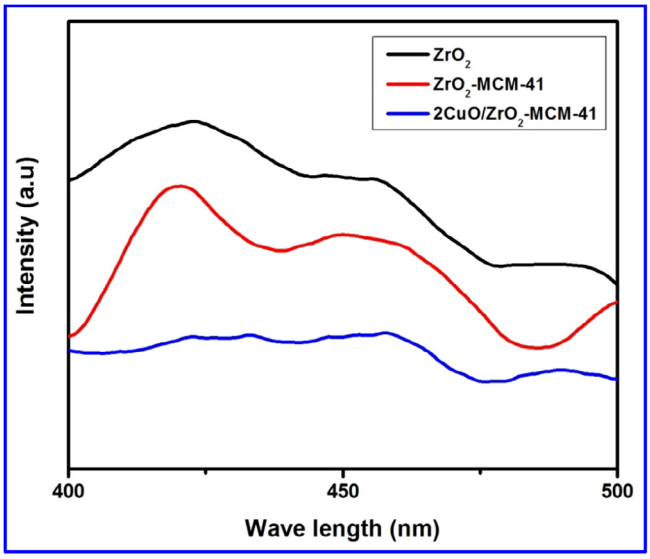

Fig. 10. Photoluminescence emission spectra of ZrO_2, mesoporous ZM-41 and CuO@ZM-41 measured at room temperature with 400 nm wavelength excitation.

Table 2
Comparison study of various catalysts on photo reduction of Cr^{6+}.

Catalyst	Concentration (mg/L)	pH	Time(min)	% of reduction	References
αFeOOH/RGO	10	2	180	94	[20]
$Gd(OH)_3$ nanorod/RGO	10	3	120	96	[21]
TiO_2, ZnO, and CdS nanoparticle	20	3	180	80	[22]
G-Fe_3O_4 and Au/G-Fe_3O_4	10	–	60	95	[23]
TiO_2 pillared ZiP and TiP	20	2	240	96	[24]
SO_4^{2-} modified TiO_2	20	3	180	94	[25]
Amine functionalized TiO_2	48	2	60	94	[26]
CuO@ZM-41	20	4	30	99	Present work

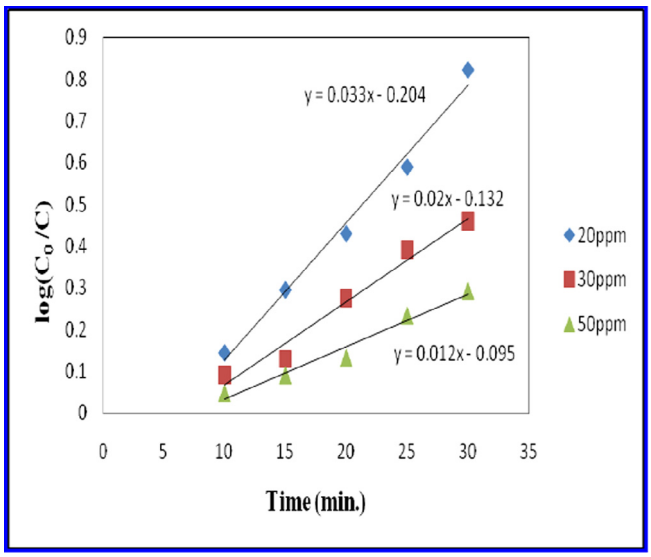

Fig. 11. Plot of log C_0/C vs. time for photo-reduction of Cr^{6+}: (a) 2 CuO@ZM-41 catalyst dose = 1.0 g L^{-1}, pH = 4.0, Cr^{6+} = 20 mg L^{-1}.

formation of nanoparticle and presence of less amount of Cu particle. So, in 2 CuO@ZM-41, the photo induced charge carriers can migrate easily and thus recombination rate greatly decreased.

3.10. Kinetic analysis

The kinetic study of different concentrations of Cr^{6+} for photo-reduction (20, 30 and 50 mg L^{-1}) process over 2 CuO@ZM-41 with different time intervals (10, 15, 20, 25 and 30 min) is shown in Fig. 11. Photo-reduction process gradually decreases with increase in Cr^{6+} concentration, already explained in the supporting information Fig. SI 3. There is a interrelation between concentration of $Cr^{6+}$and irradiation time. The photo-reduction of Cr^{6+} followed the 1st order reaction kinetics.

$$\text{Log } C_0/C = Kt/2.303 \quad (9)$$

$$K = \log C_0/C \times 2.303/t \quad (10)$$

where Kapp is the 1st order apparent rate constant, C_0 is the initial concentration of Cr^{6+} and C is the concentration at time t in Eqs. (5) and (6). With increase in Cr^{6+} concentration from 20 to 50 mg L^{-1} the Kapp values were found to decrease. The (Kapp) value of Cr^{6+}at 30 min time is presented in Table 3.

3.11. Stability and prove of photo-reduction

Besides the photo-reduction activity, the stability study of catalyst is important for different applications which are shown in Fig. 12(a). The stability of the mesoporous CuO@ZM-41 composite was evaluated by performing recycling experiments on the photo-reduction under similar conditions. The activity was found to be almost same in three repeated runs and then there is slight decrease in the activity. The XPS spectrum of Cr 2p after photo-reduction of Cr^{6+} on 2 CuO@ZM-41 is shown in the Fig. 12(b). It has been noted that the Cr $2p_{3/2}$ and Cr $2p_{1/2}$ at binding energy of 579.4 and 586.6 eV, respectively, were very closed to the of Cr 2p peaks in $K_2Cr_2O_7$ which suggested the Cr^{6+} [51,52]. But from Fig. 12(b), the photoelectron peaks at 577.8 and 588.2 eV correspond to the binding energies of Cr $2p_{3/2}$ and Cr $2p_{1/2}$ for Cr^{3+} [53,54]. This may be due to presence of Cr^{3+} after photo-reduction from Cr^{6+} on the surface of 2 CuO@ZM-41. This result

Table 3
Rate kinetic of Cr^{6+} reduction on 2CuO@ZM-41.

Time	Concentration (20 mg/L)		Concentration (30 mg/L)		Concentration (50 mg/L)	
	Photo-reduction (%)	log C_0/C	Photo-reduction (%)	log C_0/C	Photo-reduction (%)	log C_0/C
10	28.33	0.144	16.9	0.089	10.3	0.47
15	36.2	0.295	25.6	0.128	18.7	0.08
20	50.35	0.430	37.4	0.273	26.2	0.13
25	63.2	0.590	46.0	0.389	41.6	0.23
30	85.0	0.823	65.2	0.458	49.0	0.29

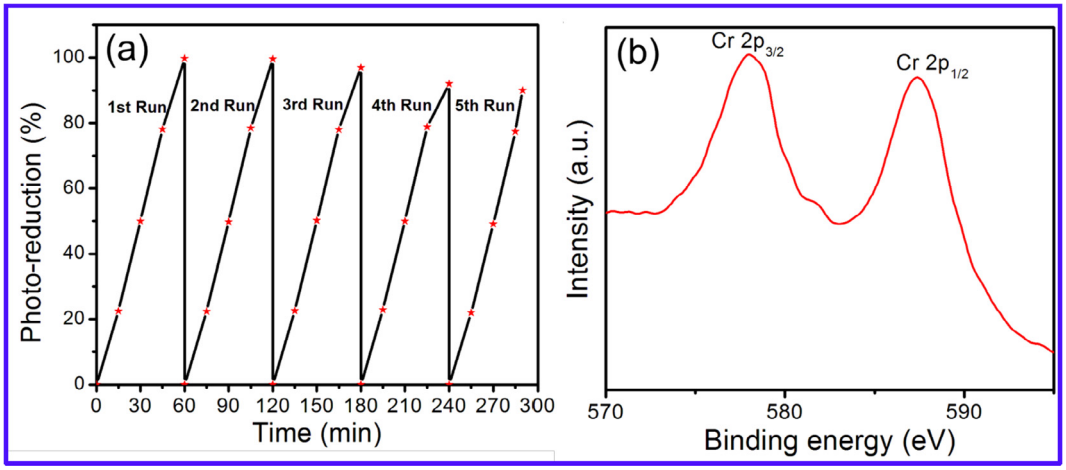

Fig. 12. (a) Recycling study of Cr^{6+} by using 2 CuO@ZM-41 in the optimum condition, (b) Core level XPS spectrum of Cr 2p after photo-reduction on 2 CuO@ZM-41.

prove that Cr^{6+} reduced completely to Cr^{3+} during photo-reduction on 2 CuO@ZM-41.

4. Conclusions

The surface modification of mesoporous ZM-41 with CuO generates highly efficient 2 CuO@ZM-41 photocatalysts. The mesoporous nanocomposite material (2 CuO@ZM-41) exhibits high photo reduction activity towards Cr^{6+} reduction. The rate of photo-reduction of Cr^{6+} followed first order reaction rate kinetics .The incorporation of Cu(II) onto the mesoporous support ZM-41 enhances the surface anchoring sites because of the development of synergism between metal to support material. The high surface area, intra-particle mesoporosity of mesoporous ZM-41 support, presence of well dispersed CuO nano rods, electron transfer ability, development of synergism between metal and support material and reduced e^{-}-h^{+} recombination which combined enhances the photo-reduction of Cr^{6+} to Cr^{3+} in 30 min. The catalyst is eco-friendly, cost effective, reusable and effective photocatalyst and potential to be explored for the abatement of environmental pollution problem.

Acknowledgement

Authors are extremely grateful to the management of SOA University for their encouragement and kind support.

Appendix A. Supplementary data

Supplementary data associated with this article can be found, in the online version, at http://dx.doi.org/10.1016/j.cej.2016.11.080.

References

[1] J. Pradhan, S.N. Das, R.S. Thakur, Adsorption of hexavalent chromium from aqueous solution by using activated red mud, J. Colloid Interface Sci. 217 (1999) 137–141.
[2] Y.N. Chen, L.Y. Chai, Bioinformatics and Biomedical Engineering Conference Proceedings, vol. 16, 2008, pp. 3248–3251.
[3] L.E. Eary, R. Dhanpat, Chromate removal from aqueous wastes by reduction with ferrous ion, Environ. Sci. Technol. 22 (1988) 972–977.
[4] T.K. Yurik, A.K. Pikaev, Radiolysis of weakly acidic and neutral aqueous solutions of hexavalent chromium ions, High Energy Chem. 33 (1999) 208–212.
[5] M. Costa, Toxicity and carcinogenicity of Cr (VI) in animal models and humans, Crit. Rev. Toxicol. 27 (1997) 431–442.
[6] M.E. Losi, C. Amrhein Jr., W.T. Frankenberger, Environmental biochemistry of chromium, Rev. Environ. Contam. Toxicol. 136 (1994) 91–121.
[7] Q. Rongliang, Z. Dongdong, Z.D. Zenghui, H. Xiongfei, H. Chun, M. Jean-Louis, X. Ya, Visible light induced photocatalytic reduction of Cr (VI) over polymer-sensitized TiO_2 and its synergism with phenol oxidation, Water Res. 46 (2012) 2299–2306.
[8] S. Wang, Z. Wang, Q. Zhung, Photocatalytic reduction of the environmental pollutant Cr^{VI} over a cadmium sulphide powder under visible light illumination, Appl. Catal. B Environ. 1 (1992) 257–270.
[9] K.M. Parida, K.G. Mishra, S.K. Dash, Adsorption of toxic metal ion (Cr (VI)) from aqueous state by TiO_2–M-41: equilibrium and kinetic studies, J. Hazard. Mater. 241 (2012) 395–403.
[10] S. Mallick, S.S. Dash, K.M. Parida, Adsorption of hexavalent chromium on manganese nodule leached residue obtained from NH_3-SO_2 leaching, J. Colloid Interface Sci. 297 (2006) 419–425.
[11] Y. Zhang, J. Crittenden, D.W. Hand, The solar photocatalytic decontamination of water, Chem. Ind. 19 (1994) 714–717.
[12] J. Galvez, S.W. Rodriguez, Proceedings of the International Conference on Comparative Assessments of Solar Power Technologies, vol. 14, 1994, p. 1.
[13] A. Okabe, T. Fukushima, K. Ariga, M. Niki, T. Aida, Tetra fluoroborate salts as site-selective promoters for sol–gel synthesis of mesoporous silica, J. Am. Chem. Soc. 126 (2004) 9013–9016.
[14] A. Vinu, V. Murugesan, M. Hartmann, Pore size engineering and mechanical stability of the cubic mesoporous molecular sieve SBA-15, Chem. Mater. 15 (2003) 1385–1393.
[15] C. Song, K.M. Reddy, Mesoporous molecular sieve M-41 supported Co–Mo catalyst for hydrodesulphurization of dibenzo thiophene in distillate fuels, Appl. Catal. A 176 (1999) 1–10.
[16] C.A. Koh, R. Nooney, S. Tahir, Characterisation and catalytic properties of M-41 and Pd/M-41 materials, Catal. Lett. 47 (1997) 199–203.
[17] J. Yu, Z. Feng, L. Xu, M. Li, Q. Xin, Z. Liu, C. Li, Ti–M-41 synthesized from colloidal silica and titanium trichloride: synthesis, characterization, and catalysis, Chem. Mater. 13 (2001) 994–998.
[18] D. Rath, K.M. Parida, Copper and nickel modified MCM-41 an efficient catalyst for hydro de halogenation of chloro benzene at room temperature, Ind. Eng. Chem. Res. 50 (2011) 2839–2849.
[19] D.W. Chen, M. Sivakumar, A.K. Ray, Semiconductor photocatalysis in environmental remediation Dev, Chem. Eng. Miner. Process. 8 (2000) 505–550.
[20] D.K. Padhi, K.M. Parida, Facile fabrication of α-FeOOH nanorod/RGO composite: a robust photocatalyst for reduction of Cr^{6+} under visible light irradiation, J. Mate. Chem. A. 26 (2014) 10300–10312.
[21] D.K. Padhi, G.K. Pradhan, K.M. Parida, S.K. Singh, Facile fabrication of Gd $(OH)_3$ nanorod/RGO composite: synthesis, characterisation and photocatalytic reduction of Cr (VI), Chem. Eng. J. 255 (2014) 78–88.
[22] K.M. Joshi, V.S. Shrivastava, Photocatalytic degradation of chromium (VI) from wastewater using nanomaterials like TiO_2, ZnO, and CdS, Appl. Nanosci. 1 (2011) 147–155.
[23] P.M. Mishra, G.K. Naik, A. Nayak, K.M. Parida, Facile synthesis of nano-structured magnetite in presence of natural surfactant for enhanced photocatalytic activity for water decomposition and Cr6+ reduction, Chem. Eng. J. 299 (2016) 227–235.
[24] D.P. Das, K.M. Parida, B.R. De, Photocatalytic reduction of hexavalent chromium in a solution over titania pillared zirconium phosphate and titanium phosphate under solar radiation, J. Mol. Catal. A. Chem. 245 (2006) 217–224.
[25] P. Mohapatra, S.K. Samantaray, K.M. Parida, Photocatalytic reduction of hexavalent chromium in aqueous solution over sulphate modified titania, J. Photochem. Photobiol. A 170 (2005) 189–194.
[26] H. Wanga, X. Yuana, Y. Wuc, G. Zenga, X. Chend, L. Lenga, Z. Wua, L. Jianga, H. Lie, Facile synthesis of amino-functionalized titanium metal-organic frameworks and their superior visible-light photocatalytic activity for Cr(VI) reduction, J. Hazard. Mater. 286 (2015) 187–194.
[27] K.V.R. Chary, B.R. Rao, V.S. Subrahmanyam, Characterization of supported vanadium oxide catalysts by a low-temperature oxygen chemisorption technique: III TheV_2O_5/ ZrO_2system, Appl. Catal. 7 (1991) 1–13.
[28] T. Yamaguchi, Application of ZrO_2 as a catalyst and a catalyst support, Catal. Today 20 (1994) 199–217.
[29] K. Tanabe, T. Yamaguchi, Acid-base bifunctional catalysis by ZrO_2 and its mixed oxides, Catal. Today 20 (1994) 185–197.
[30] S. Rana, S. Mallick, K.M. Parida, A facile method for synthesis of polyamine-functionalized mesoporous zirconia and its catalytic evaluation towards Henry reaction, Ind. Eng. Chem. Res. 50 (2011) 2055–2064.
[31] S. Mallick, S. Rana, K.M. Parida, A facile method for the synthesis of copper modified amine-functionalized mesoporous zirconia and its catalytic evaluation in C-S coupling reaction, Dalton Trans. 40 (2011) 9169–9175.
[32] E. Pardo, P. Burguete, R. Ruiz-Garcia, M. Julve, D. Beltran, Y. Journaux, P. Amoros, F. Lioret, Ordered mesoporous silicas as host for the incorporation and aggregation of octa nuclear nickel (II) single-molecule magnets: a bottom-up approach to new magnetic nanocomposite materials, J. Mater. Chem. 16 (2006) 2702–2714.
[33] A. Miko, D. Levent, M. Somer, Vertically oriented hexagonal mesoporous zirconia thin films by block copolymer templating, J. Mater. Chem. 22 (2012) 3705–3707.
[34] S. Qin, F. Xin, Y. Liu, W. Ma, Photocatalytic reduction of CO_2 in methanol to methyl formate over CuO-TiO_2 composite catalysts, J. Colloid Interface Sci. 356 (2011) 257–261.
[35] A.C. Pradhan, K.M. Parida, B. Nanda, Enhanced photocatalytic and adsorptive degradation of organic dyes by mesoporous Cu/Al_2O_3–MCM-41:intra-particle mesoporosity, electron transfer and OH radical generation under visible light, Dalton Trans. 40 (2011) 7348–7356.
[36] S. Brunauer, P.H. Emmt, E. Teller, Adsorption of gases in multimolecular layers, J. Am. Chem. Soc. 60 (1938) 309–319.
[37] A.C. Pradhan, S. Martha, S.K. Mahanta, K.M. Parida, Mesoporous nanocomposite Fe/Al_2O_3–MCM-41: An efficient photocatalyst for hydrogen production under visible light, Int. J. Hydrogen Energ. 36 (2011) 12753–12760.
[38] N. Srinivas, V. Radha Rani, S.J. Kulkarni, K.V. Raghavan, Liquid phase oxidation of anthracene and trans-stilbene over modified mesoporous (M-41) molecular sieves, J. Mol. Catal. A Chem. 179 (2002) 221–231.
[39] M. Mizuno, Y. Sasaki, S. Lee, H. Katakura, High-yield sol–gel synthesis of well-dispersed, colorless ZrO_2 nanocrystals, Langmuir 22 (2006) 7137–7140.
[40] M. Chun, M.J. Moon, J. Park, Y.C. Kang, Physical and chemical investigation of substrate temperature dependence of zirconium oxide films on Si (100), Bull. Korean Chem. Soc. 30 (2009) 112729–112734.
[41] B. Nanda, A.C. Pradhan, K.M. Parida, A comparative study on adsorption and photocatalytic dye degradation under visible light irradiation by mesoporous MnO_2 modified MCM-41 nanocomposite, Microporous Mesoporous Mater. 226 (2016) 229–242.
[42] M.C. Marion, E. Garboeski, M.J. Primet, Physicochemical properties of copper oxide loaded alumina in methane combustion, Chem. Soc. Faraday Trans. 87 (1991) 1795–1800.
[43] K.M. Parida, D. Rath, Structural properties and catalytic oxidation of benzene to phenol over CuO-impregnated mesoporous silica, Appl. Catal. A 11 (2007) 101–108.

[44] M. Shimokawabe, H. Asakawa, N. Takezawa, Characterization of copper/zirconia catalysts prepared by an impregnation method, Appl. Catal. 59 (1990) 45–58.
[45] A.C. Pradhan, B. Nanda, K.M. Parida, G.R. Rao, Fabrication of the mesoporous Fe@MnO_2NPs–MCM-41 nanocomposite: an efficient photocatalyst for rapid degradation of phenolic compounds, J. Phys. Chem. C 119 (2015) 14145–14159.
[46] K. Dimos, P. Stathi, M.A. Karakassides, Y. Deligiannakis, Synthesis and characterization of hybrid MCM-41 materials for heavy metal adsorption, Microporous Mesoporous Mater. 126 (2009) 65–71.
[47] S. Mansingh, D.K. Padhi, K.M. Parida, Enhanced photocatalytic activity of nanostructured Fe doped CeO for hydrogen production undervisible light irradiation, J. Hydrogen Energy 41 (2016) 14133–14146.
[48] X. Li, M. Antonietti, Metal nanoparticles at mesoporous N-doped carbon and carbon nitrides: functional Mott-Schottky heterojunctions for catalysis, Chem. Soc. Rev. 42 (2013) 6593–6604.
[49] V. Nieminen, H. Karhu, N. Kumar, I. Heinmaa, P.E.A. Samoson, T. Salmia, D.Y. Murzin, Physico-chemical and catalytic properties of Zr- and Cu–Zr ion-exchanged H-M-41, Phys. Chem. Chem. Phys. 6 (2004) 4062–4069.
[50] K.H. Reddy, S. Martha, K.M. Parida, Fabrication of novel p-BiOI/n-ZnTiO3 hetero junction for degradation of rhodamine 6G under visible light irradiation, Inorg. Chem. 52 (2013) 6390–6401.
[51] L.G. Yan, K. Yang, R.R. Shan, H.Q. Yu, B. Du, Calcined ZnAl- and Fe_3O_4/ZnAl–layered double hydroxides for efficient removal of Cr (VI) from aqueous solution, RSC Adv. 5 (2015) 96495.
[52] A.R. Di Sarli, J.D. Culcasi, C.R. Tomachuk, C.I. Elsner, J.M. Ferreira-Jr, I. Costa, A conversion layer based on trivalent chromium and cobalt for the corrosion protection of electro galvanized steel, Surf. Coat. Technol. 258 (2014) 426–436.
[53] B. Manning, J. Kiser, H. Kwon, S.R. Kanel, Spectroscopic investigation of Cr (III)- and Cr (VI)-Treated nanoscale zero valent iron, Environ. Sci. Technol. 41 (2007) 586–592.
[54] H. Jabeen, V. Chandra, S. Jung, J.W. Lee, K.S. Kim, S.B. Kim, Enhanced Cr(VI) removal using iron nanoparticle decorated grapheme, Nanoscale 3 (2011) 3583.